Northumbria Research Link

Northumbria
University
NEWCASTLE

University**Library**

Optical OFDM Based on Fractional Fourier Transform for an Indoor VLC System

MAHDI NASSIRI,[1] GHOLAMREZA BAGHERSALIMI,[1,*] AND ZABIH GHASSEMLOOY [2]

[1] Department of Electrical Engineering, University of Guilan, Rasht, Iran
[2] Optical Communications Research Group, Faculty of Engineering and Environment, Northumbria University, Newcastle, UK
*Corresponding author: bsalimi@guilan.ac.ir

The fractional Fourier transform (FRFT), which is a family of linear transformations generalizing the classical Fourier transform, has been used in the fields of filter design, signal processing, phase retrieval, and pattern recognition due to its unique properties. The FRFT of a signal can be interpreted as a decomposition of the signal in terms of chirps. In this paper, for the first time we introduce an optical FRFT (OFRFT)-based orthogonal frequency division multiplexing (OFDM) visible light communications (VLC) system and compare numerical results with a direct current-biased optical (DCO)-OFDM system. Firstly, the optimal fractional order is calculated to improve the performance of the proposed system by minimizing the bit error rate (BER). The numerical results show that, OFRFT-OFDM with the optimal fractional order offers a significantly improved BER performance compared with DCO-OFDM under the same computational complexity and spectral efficiency. In addition, the peak to average power ratio, which is an issue in light emitting diode-based VLC systems, is reduced by < 1 dB using OFRFT-OFDM for the same BER compared with DCO-OFDM.

1. Introduction

Future smart environments (i.e., networks concept) will build on the required scientific and technological advances in the areas of key enabling wireless technologies to provide a coherent framework in supporting massive Internet of things (IoT). The availability of frequency spectrum is one of the main factors, which will determine the system capacity. However, the radio frequency (RF) spectrum is a scarce resource especially the lower frequency bands, which are limited and tightly regulated. Therefore, new high data rate multimedia services and applications that are being developed at a large scale are putting tremendous pressure on the existing RF-based wireless technologies and have resulted in spectral congestion (or bandwidth bottleneck). In addition, the RF technologies have other drawbacks such as lower data rates, costly spectrum licensing, low level of security and high installation cost [1, 2]. The fifth generation (5G) and beyond wireless network is aiming to address these challenges, however there is still the need for complementary technologies, which can release the pressure on the spectrum usage in RF systems in certain applications. To satisfy the high bandwidth demands of upcoming multimedia type services using wireless systems, there are number of options including reutilization of the existing spectrum resources, more advanced modulation and multiplexing schemes, cell densification,

parallel transmission, and higher carrier frequencies. The latter includes millimeter wave (mmW), terahertz, and optical waves. The 5G wireless networks aim to use mmW in mobile networks [3]. However, the RF part of the electromagnetic spectrum will not be sufficient to support data-driven economies and societies. It is, therefore, natural to move to the light carrier frequencies by using the optical wireless communication (OWC) technologies, which includes infrared, visible and ultraviolet spectrum bands. OWC offers features, which are complementary to RF, including license free, virtually unlimited bandwidth for providing near-optimal capacity as in optical fiber communications, security and low installation cost [1, 4]. In addition, the appealing advantage of achieving high energy efficiency and high-speed data communications will become even more important in device-to-device communications. The visible band (370-780 nm) in OWC is best known as visible light communications (VLC), which has attracted growing research interests in the last decade, that utilizes the light emitting diodes (LEDs)-based lighting fixtures in indoor (and to some extent in outdoor) environments for illumination, data communication, sensing and indoor positioning [5-8]. In recent years, the major research efforts have been focused on enhancing transmission data rates of intensity modulation/direct detection (IM/DD) VLC systems, but over a very short transmission link spans (e.g., less than one meter) [9].

In VLC systems, the transmission data rate is mainly determined by the modulation bandwidth of the LED, which can vary within the range of a few MHz to ~ 100 MHz depending on the type of the device being used [9]. To address this issue, possible options have been investigated including equalization, and multi-level and multi-carrier (MC) modulation schemes. One attractive and resilient MC scheme, which has been migrated from the RF wireless systems (4G/5G), is the orthogonal frequency division multiplexing (OFDM) [10, 11]. Furthermore, in OFDM (*i*) equalization can be performed using a single-tap equalizer (EQ) in the frequency domain (FD), which reduces the design complexity and implementation cost; and (*ii*) different frequency subcarriers (SCs) can be adaptively loaded with the data based on the free space channel characteristics [12]. The conventional OFDM signals are both bipolar and complex-valued, which needs to be real and unipolar for IM/DD optical systems. Hermitian symmetry on the SCs in the FD has been used to achieve a real-valued OFDM signal. As for bipolarity of the OFDM signal, a number of possible approaches have been proposed including direct current-biased optical OFDM (DCO-OFDM), asymmetrically clipped optical OFDM (ACO-OFDM), pulse-amplitude-modulated discrete multitone modulation (PAM-DMT), and unipolar OFDM (U-OFDM) [9, 12].

In OFDM, the equally spaced and overlapping SCs are orthogonal and thus free from the intersymbol interference (ISI). However, the performance of conventional OFDM will be degraded due the carrier frequency offset (CFO), Doppler shift, phase noise, nonlinear effects, and chromatic dispersions (CDs). Alternatively, OFDM based on orthogonal chirped SCs, namely the fractional Fourier transform (FRFT), has been reported in the literature [13-16], which is a generalization of Fourier transform (FT) for filling the gap between the time and frequency domains. The FT can be interpreted as the projection of a given signal on the frequency axis, i.e., a rotation of $\pi/2$ with respect to the time axis, while FRFT can be defined as the projection of the signal on an axis that forms an angle $p\pi/2$ with $0 < |p| < 2$, i.e., a rotation in the time-frequency plane. Note that, FRFT can be electronically implemented with a complexity equivalent to the traditional fast FT (FFT) [15-17].

In [15], it was shown that the computational complexity, optical implementation, and the spectral efficiency η_{se} of FRFT-based OFDM are almost identical to the conventional FT. In addition, it was stated that the chirped SC decomposition is a powerful tool to compensate for the CD and to reduce the peak to average power ratio (PAPR) requirement. In [18], FRFT was introduced for the first time followed by the investigation of FRFT in its time-frequency domain [19]. FRFT was first applied in MC systems in [20]. In [21], a method of measuring the CD in an optical fiber link based on the optimal fractional order and using FRFT was proposed, where coherent demodulation was used to obtain the complex field of the optical pulse signal followed by FRFT on the complex field based on the energy focusing effect of the chirp signal in the fractional spectrum. The authors in [22] demonstrated a blind CD estimation method based on the FRFT with lower computational complexity

and improved robustness to transmission impairments compared with other CD estimation schemes. Through numerical simulations, their proposed CD estimation method showed a robust performance against amplified spontaneous emission noise and fiber nonlinearity. Authors in [23] introduced a novel in-band optical signal to noise ratio monitoring technique in a digital coherent receiver (Rx) based on FRFT, where the power aggregation property of linear frequency modulation signal was used in the fractional domain.

FRFT-based OFDM systems have been adopted in RF [24, 25], optical fiber [15, 22, 26], and underwater acoustic communication systems [16, 27]. LEDs are the most critical component in VLC systems due to their limited modulation bandwidth and nonlinear power-current characteristic. The FRFT-OFDM system has been reported in the literature, which offers improved performance in nonlinear or frequency-selective systems. Thus, the use of FRFT-OFDM in place of FFT-OFDM in LED-based VLC systems can be effective to improve the performance. However, to the best of the authors' knowledge, FRFT-OFDM has not yet been investigated in OWC systems and particularly in VLC. In this paper, we propose an optical FRFT-based OFDM (OFRFT-OFDM) system and evaluate and compare its performance with the conventional DCO-OFDM. The results show that OFRFT-OFDM with the optimal fractional order offers a significantly improved bit error rate (BER) performance compared with DCO-OFDM with the same computational complexity and η_{se}. OFRFT-OFDM also offers lower PAPR, which is a crucial issue in LED-based VLC systems, compared with DCO-OFDM.

The rest of the paper is organized as follows. Section 2 comprehensively describes the foundations of the proposed OFRFT-OFDM system and provides its mathematical analysis. Significant results and discussion are presented in Section 3. Eventually, Section 4 is assigned to conclude the paper.

2. System Model

In this section, we first formulate the OFRFT-based OFDM system and then explain its functionality. The goal is to compare its performance with DCO-OFDM system under the same conditions.

A. Fractional Fourier Transform

FRFT can be considered as generalized FT. If conventional FT is considered as a $\pi/2$ rotation from the time axis to the frequency axis, then FRFT can be considered as rotation with any angle α from the time domain (TD) to the FD [15, 16]. FRFT of the order p is defined as:

$$X_p(u) = \{F^p[x(t)]\}(u) = \int_{-\infty}^{\infty} x(t)K_p(t,u)dt, \qquad (1)$$

where the kernel of FRFT is given as:

$$K_p(t,u) = \begin{cases} \sqrt{1-j\cot\alpha}\,\exp[j\pi(u^2\cot\alpha - 2ut\csc\alpha + t^2\cot\alpha)], & \alpha \neq n\pi \\ \delta(t-u), & \alpha = 2n\pi \\ \delta(t+u), & \alpha = (2n+1)\pi \end{cases}, \qquad (2)$$

where $\alpha = p\pi / 2$ is the angle of rotation and F^p is the symbol of the pth order FRFT operator. Note, for $p = 1$, FRFT becomes as FT. The inverse FRFT (IFRFT) of the order p is equal to the FRFT of order $-p$, which is expressed as [16]:

$$x(t) = \int_{-\infty}^{\infty} X_p(u) K_{-p}(t, u) du. \tag{3}$$

For numerical analysis, numerous algorithms for discrete FRFT have been reported in literature. In [28], it was shown that it is possible to determine the digital FRFT with a complexity order of $O(N \log N)$, where N is the data size. In this work, we have adopted FRFT in the matrix form from [16] and references within, which is given as:

$$X_p = F_p x, \tag{4}$$

where F_p is the N-dimensional discrete FRFT matrix with components given by:

$$F_p(m, n) = \begin{cases} A_p \rho_{m^2} W_{mn} \rho_{n^2}, & p \neq 2k \\ I_{N \times N}, & p = 4k \\ J_{N \times N}, & p = 4k + 2 \end{cases}, \tag{5}$$

where $A_p = \sqrt{(\sin\alpha - j\cos\alpha)/N}$, $\rho_{m^2} = \exp(j\,0.5\cot\alpha\Delta u^2 m^2)$, $W_{mn} = \exp(-j\,2\pi mn / N)$, $\rho_{n^2} = \exp(j\,0.5\cot\alpha\Delta t^2 n^2)$, $m, n = 0, 1, ..., N-1$, k is an integer, Δt is the time interval, and Δu is the interval between samples in the pth order FRFT. $I_{N \times N}$ and $J_{N \times N}$ are the N-dimensional identity and exchange matrices, respectively. Note that, there is a constraint between Δt and Δu to ensure a reversible condition, which is expressed as:

$$\Delta u = \frac{2\pi |\sin\alpha|}{N \Delta t}. \tag{6}$$

The discrete IFRFT is given as:

$$x = F_{-p} X, \tag{7}$$

where $F_{-p} = F_p^H$ is defined as:

$$F_{-p}(n, m) = \begin{cases} \rho_{-n^2} W_{-nm} \rho_{-m^2} A_p^*, & p \neq 2k \\ I_{N \times N}, & p = 4k \\ J_{N \times N}, & p = 4k + 2 \end{cases}, \tag{8}$$

where $(.)^H$ indicates Hermitian transpose of matrix.

B. Reality Preserving FRFT

FRFT with the real-valued data results in complex-valued outputs. In IM/DD VLC systems, OFDM signal needs to be real and unipolar, where the latter is achieved using DC-biasing. To ensure that the output of FRFT is real, a new form of FRFT is needed, which can map a real set to another real set. In [29], a methodology for obtaining the variants of discrete fractional cosine (sine) transform was proposed, which shared real-valuedness, decentralization, and most of the properties required in a fractional transform matrix. In this work, we have adopted the techniques introduced in [29, 30] to construct the reality-preserving FRFT (RPFRFT).

Let $x = \{x_1, x_2, x_3, ..., x_N\}^T$ be a real signal of length N, which is an even number, and F_p be the complex valued discrete FRFT matrix of size $N/2$. In addition, let $x = \{x_1 + ix_{(N/2)+1}, x_2 + ix_{(N/2)+2}, ..., x_{N/2} + ix_N\}^T$ of length $N/2$ be a complex vector constructed from x. For x applied to the FRFT matrix we have:

$$\begin{aligned} y &= F_p x = [\text{Re}(F_p) + i\text{Im}(F_p)].[\text{Re}(x) + i\text{Im}(x)] \\ &= [\text{Re}(F_p).\text{Re}(x) - \text{Im}(F_p).\text{Im}(x)] \\ &\quad + i[\text{Re}(F_p).\text{Im}(x) + \text{Im}(F_p).\text{Re}(x)] \end{aligned} \tag{9}$$

Then, the real and imaginary parts of y can be separated as:

$$\begin{aligned} y &= \begin{bmatrix} \text{Re}(F_p).\text{Re}(x) - \text{Im}(F_p).\text{Im}(x) \\ \text{Re}(F_p).\text{Im}(x) + \text{Im}(F_p).\text{Re}(x) \end{bmatrix} \\ &= \begin{bmatrix} \text{Re}(F_p) & -\text{Im}(F_p) \\ \text{Im}(F_p) & \text{Re}(F_p) \end{bmatrix} . \begin{bmatrix} \text{Re}(x) \\ \text{Im}(x) \end{bmatrix} = R_p x, \end{aligned} \tag{10}$$

where the RPFRFT matrix is given by:

$$R_p = \begin{bmatrix} \text{Re}(F_p) & -\text{Im}(F_p) \\ \text{Im}(F_p) & \text{Re}(F_p) \end{bmatrix}. \tag{11}$$

It should be noted that, (i) R_p contains the most basic properties of F_p such as orthogonality, additivity, periodicity, and commutativity; and (ii) the inverse of RPFRFT given by R_{-p}.

C. The Proposed System

Fig. 1 shows the schematic diagram of the proposed system. As can be seen, the serial input bit streams $\{I_n\}$ are converted into the phase shift keying (PSK) format $S[u]$, and the real and imaginary components of the modulated symbols applied to the serial to parallel (S/P) converters with the concatenated vector signal of $S_c[u] = [\text{Re}(S[u]), \text{Im}(S[u])]^T$ applied to RPIFRFT followed by the parallel to serial (P/S) converter the output of which is a bipolar and real-valued vector as given by:

$$\begin{aligned} s_c[n] &= R_{-p} S_c[u] \\ &= \begin{bmatrix} \text{Re}(F_{-p}) & -\text{Im}(F_{-p}) \\ \text{Im}(F_{-p}) & \text{Re}(F_{-p}) \end{bmatrix} . \begin{bmatrix} \text{Re}(S[u]) \\ \text{Im}(S[u]) \end{bmatrix} \\ &= \begin{bmatrix} \text{Re}(F_{-p}).\text{Re}(S[u]) - \text{Im}(F_{-p}).\text{Im}(S[u]) \\ \text{Im}(F_{-p}).\text{Re}(S[u]) + \text{Re}(F_{-p}).\text{Im}(S[u]) \end{bmatrix}. \end{aligned} \tag{12}$$

Next, zero padding (ZP) is applied to $s_c[n]$ by including $N_g = N/8$ zeros at the start of each OFRFT-OFDM symbol because of its lower power by a factor of N_g / N (i.e., 12.5% in this work) compared with the cyclic prefix as explained in [31].
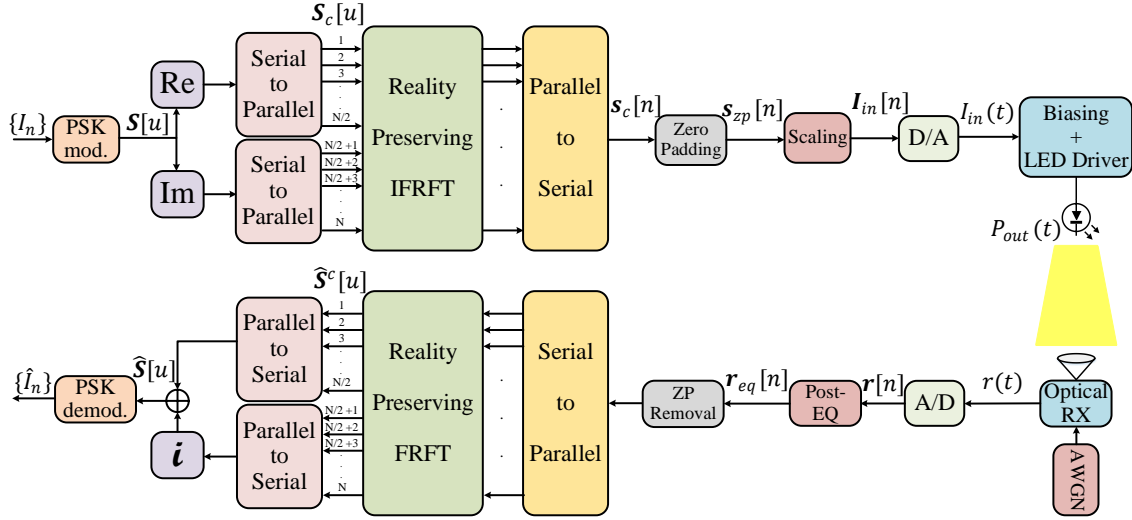
Fig. 1. The schematic block diagram of the proposed RPFRFT-OFDM system.

Following scaling of the zero padded signal $s_{zp}[n]$ due to the limited dynamic range of the LED, we have:

$$I_{in}[n] = \grave{o} s_{zp}[n]. \qquad (13)$$

where $\grave{o}$ is defined as [32]:

$$\grave{o} = \frac{\zeta I_{max}}{(\zeta + 1).max\{|s_{zp}[n]|\}}, \qquad (14)$$

so that $I_{max} = I_{DC} + 0.5 I_{pp}$ is the maximum value of $I_{in}[n]$, I_{DC} is the DC-bias current, I_{pp} is the peak-to-peak current, and ζ is the modulation index, which is defined as:

$$\zeta = \frac{I_{max} - I_{DC}}{I_{DC}}. \qquad (15)$$

Several methods have been reported in the literature to model the LED nonlinear characteristic including Volterra series [33], memory polynomial [34], Wiener [35], Hammerstein [36], etc. In this work we have adopted the most widely used Hammerstein model, which comprises a nonlinear function followed by a linear component, see Fig. 2(a). The LED nonlinearity and its impulse response are modeled as a third order polynomial, which is adopted from experimental measurements in [12], and a first order low-pass filter [9], respectively as given by Eq. (16), where B_m is the modulating bandwidth. The power-current characteristic and frequency response of the LED used in this paper are depicted in Figs. 2(b) and (c), respectively. The output power of the intensity modulated LED is given by:

$$P_{out}(t) = f_{NL}(I_{in}(t)) \otimes h_{LED}(t), \qquad (17)$$

where $I_{in}(t)$ is the continuous form of $I_{in}[n]$ and $\otimes$ indicates the TD convolution.

The free space channel is composed of line of sight (LOS) and diffuse or non-LOS (NLOS) paths as given by [37]:

$$\begin{aligned} h_{VLC}(t) &= h_{LOS}(t) + h_{NLOS}(t) \\ &= T(\phi)\frac{A_r}{d^2}\cos(\theta)\delta(t - \frac{d}{c}) + \sum_{k=1}^{\infty} h^k(t), \end{aligned} \qquad (18)$$

where ϕ and θ are the radiant angle of the transmitter (Tx) and the incident angle of the Rx, respectively. A_r, d and c are the surface area of the photodiode (PD), the LOS path length and the speed of light, respectively. $T(\phi)$ is the luminous intensity, which is given by:

$$T(\phi) = \frac{m+1}{2\pi}\cos^m(\phi), \qquad (19)$$

where m is Lambertian order, which depends on the semi-angle at half power $\phi_{1/2}$ of the LED as defined by:

$$m = \frac{-\ln(2)}{\ln(\cos(\phi_{1/2}))}. \qquad (20)$$

In this paper, for NLOS paths we have adopted the iterative site-based method as in [37]. Firstly, the surfaces of all the walls are divided into L_R small areas, which are assumed to be Lambertian reflectors with a specific reflectivity, and therefore can be viewed as both the Rx and the Tx. The impulse response of the rays between the Tx and the Rx undergoing kth-order reflection is given by Eq. (21):

$$f_{NL}(x) = \begin{cases} 0.1947, & x < 0.1 \\ 0.2855x^3 - 1.0886x^2 + 2.0565x - 0.0003, & 0.1 \le x < 1, \quad (a) \\ 1.2531, & x \ge 1 \end{cases}$$

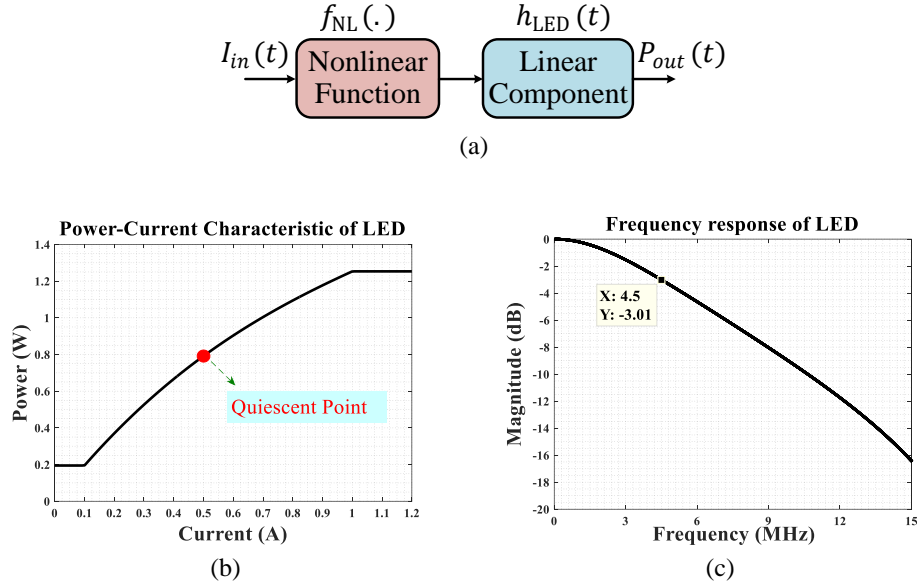$$h_{LED}(t) = e^{-2\pi B_m t}, \qquad (b)$$

(16)

Fig. 2. LED light source: (a) Hammerstein model, (b) power-current characteristic with the quiescent point of 0.5 A, and (c) frequency response with a 3-dB bandwidth of 4.5 MHz.

$$h^{(k)}(t,Tx,Rx) \cong \sum_{n=1}^{L_R} \rho_{\grave{o}_n} h^{(k-1)}(t,Tx,\grave{o}_n^r) \otimes h^{(0)}(t,\grave{o}_n^s,Rx), \quad (21)$$

where $\rho_{\grave{o}_n}$ is the reflectivity of element $\grave{o}_n$. $\grave{o}_n^r$ and $\grave{o}_n^s$ represent the nth element, acting as a Rx or a Tx, respectively. Furthermore, the LOS impulse response between $\grave{o}_n$ and the Rx is $h^{(0)}(t,\grave{o}_n^s,Rx)$. Eq. (21) can be computed iteratively for all k reflections. Nevertheless, only one reflection from the walls, i.e., $k=1$, is considered in this study. Fig. 3 shows the most important parameters used for generating the VLC channel.

Following propagation through the channel, the received optical signal is converted back into the electrical format using an optical Rx, which is a PD and a trans-impedance amplifier (TIA), i.e., $r(t) = G_{TIA}R_{PD}\{P_{out}(t) \otimes h_{VLC}(t) + n(t)\}$ where $n(t)$ is the additive white Gaussian noise (AWGN), R_{PD} is the responsivity of the PD, and G_{TIA} is the TIA gain. Next, $r(t)$ is applied to analog-to-digital (A/D) converter, the output of which is given by:

$$r[n] = [r[n], r[n-1],...,r[n-L_f+1]]^T, \quad (22)$$

where L_f is the EQ filter length. To reduce the LED bandwidth induced ISI on the received signal, $r[n]$ is applied to a linear TD-EQ with the output given as:

$$r_{eq}[n] = W^H[n]r[n], \quad (23)$$

$$e[n] = d[n] - r_{eq}[n], \quad (24)$$

$$W[n+1] = W[n] + \mu e^T[n]r[n], \quad (25)$$

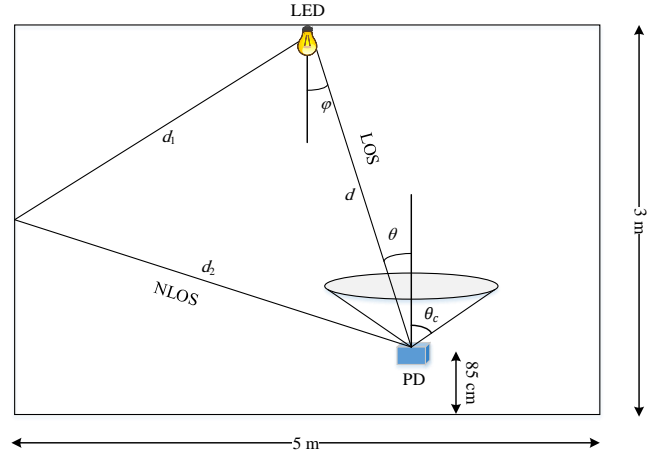
Fig. 3. The VLC link with LOS and NLOS paths.

where $e[n]$, $d[n]$ and $W[n]$ are the error, expected and weight vectors, respectively. $(.)^T$ denotes the transpose of a vector and μ is the step size. Following removal of ZP, the resultant signal is applied to RPFRFT to obtain the fractional domain. Next, the N-dimensional output of RPFRFT $S^c[u]$ is rearranged as:

$$S[u] = \left[\hat{S}_1^c[u] + i\hat{S}_{(N/2)+1}^c[u], \hat{S}_2^c[u] + i\hat{S}_{(N/2)+2}^c[u],...,\hat{S}_{N/2}^c[u] + i\hat{S}_N^c[u] \right]. \quad (26)$$

$S[u]$ is then applied to the PSK demodulator to regenerate the estimated version of the input bit stream. The resultant bit stream

$\hat{I}_n$ is compared bit-by-bit with the original data stream I_n, and the BER is the total number of errors divided by the number of transmitted bits (i.e., OFRFT-OFDM symbols).

3. Results and Discussions

In the previous section, we outlined the proposed system and showed the mathematical formulation. In this section, we present results for the OFRFT-OFDM system and compare its performance with conventional DCO-OFDM. It is worth noting that, in both systems only half of the SCs are utilized for data transmission because of Hermitian symmetry and RP, therefore the same η_{se} is achieved for both schemes. In the following, computer simulation results are presented for both systems using Matlab and the real world parameters [2, 9], see Table 1.

First, we determine the optimal order of FRFT p_{opt} by means of simulations for several FRFT orders within the range of $0.01 \leq p \leq 1.99$ using binary PSK (BPSK) with no EQs at both the Tx and the Rx. Note that, 16000 OFRFT-OFDM symbols are transmitted in this case, each carrying 64 bits, and therefore 1,024,000 bits are sent for each p. After acquiring the optimal order, channel EQ and higher orders of modulation are examined by use of this predesignated p_{opt}. Fig. 4 illustrates the BER performance as a function of fractional order p for a fixed E_b / N_0 of 20 dB. As shown, the highest and lowest BER values of 0.015 and 10^{-4} are observed for p of 1 and 0.94 corresponding to the conventional FFT and OFRFT-OFDM, respectively. Also shown is the 7% forward error correction (FEC) limit of 3.8×10^{-3}. As previously mentioned, the computational complexity of digital FRFT and FFT algorithms are the same. Hence, the fractional order belonging to the lowest BER is considered as the default value, which is $p_{opt} = 0.94$ or equivalently $\alpha_{opt} = \frac{p_{opt}\pi}{2} \approx 85°$.

Table 1. System parameters [2, 9]

| Symbol	Parameter	Value
-	Room size	5×5×3 m³
d	Distance between the Tx and the Rx	2.15 m
$\phi_{1/2}$	Semi-angle at half power	70°
θ_c	PD field of view	60°
A_r	PD surface area	1 cm²
R_{PD}	Responsivity of PD	0.54 A/W
B_m	Modulating bandwidth of LED	4.5 MHz
B_T	Total bandwidth of OFDM	5 MHz
G_{TIA}	TIA gain	50 dB
-	Modulation type	PSK
-	Tx position	(2.5, 2.5, 3) m
-	Rx position	(2.5, 2.5, 0.85) m
N	Total number of SCs	128
N_d	Number of data SCs	64
N_g	Number of ZP samples	16
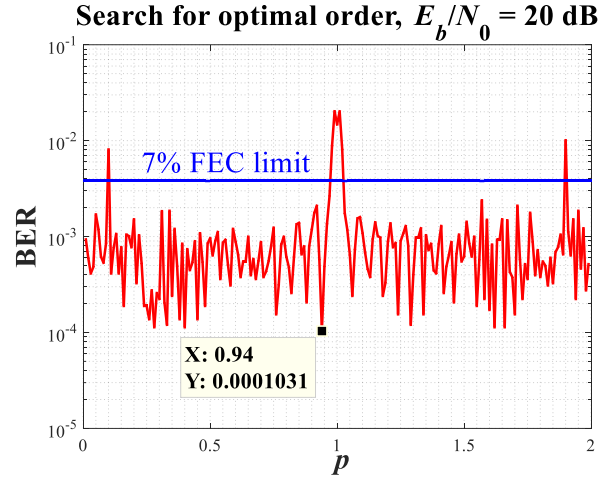
Fig. 4. The BER performance against the fractional order p of OFRFT-OFDM.

Fig. 5 depicts the BER against I_{DC} for DCO-OFDM (i.e., FFT) and OFRFT-OFDM (with p_{opt} of 0.94) systems for E_b / N_0 of 20 dB. As can be seen, OFRFT-OFDM offers much improved BER performance compared with the DCO-OFDM particularly for $0.4 < I_{DC} < 0.7$ A. The BER decreases by increasing I_{DC} reaching the minimum values of ~ 0.01 and 1.1×10^{-4} for FFT and FRFT, respectively, at I_{DC} of 550 mA and afterward, the BER for both systems increases.

In MC modulation-based VLC, the link performance will depend on the PAPR due to limited linear dynamic range of the LED and any other amplification devices. Fig. 6 illustrates the complementary cumulative distribution function (CCDF) of the PAPR as a function of the threshold $PAPR_0$ for both systems. Note that, CCDF of $PAPR_0$ is the probability that the PAPR of signal will be above the $PAPR_0$. As can be seen, for the OFRFT-OFDM the $PAPR_0$ values are lower by < 1 dB for $5 < PAPR_0 < 11$ dB compared with DCO-OFDM.
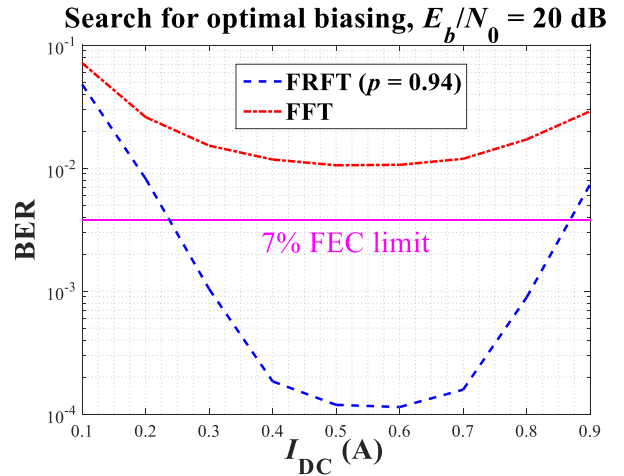

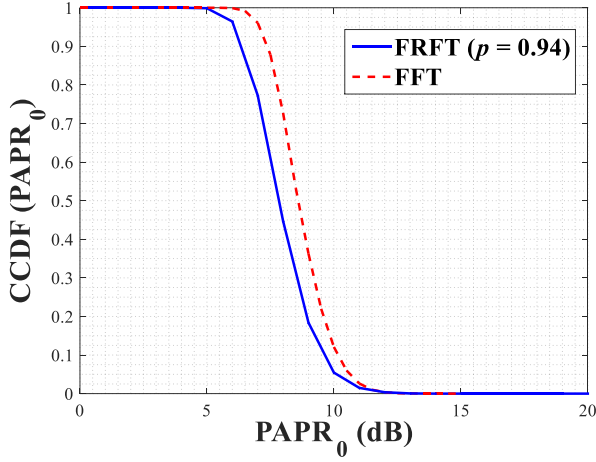Fig. 5. The BER against DC-bias for OFRFT-OFDM with optimal order and DCO-OFDM.

Fig. 6. CCDF of PAPR against the threshold $PAPR_0$ for OFRFT-OFDM and DCO-OFDM systems.

The BER performance against E_b/N_0 for both systems with and without the EQs is depicted in Fig. 7. Also shown is the theoretical BER for BPSK over an AWGN channel for comparison. As can be seen, OFRFT-OFDM with no EQ meets the 7% FEC at E_b/N_0 of ~ 12.5 dB in contrast to DCO-OFDM, which fails to do so. Note, for OFRFT-OFDM using the EQ, the required E_b/N_0 to achieve the FEC limit is reduced to ~ 11 dB (a ~ 6 dB power penalty compared with the reference plot) and there is no error floor. Also note, DCO-OFDM meets the FEC limit at E_b/N_0 of ~ 16.5 dB. Although, the performance of both systems is improved when using EQ, OFRFT-OFDM still outperforms DCO-OFDM. For instance, the BER performances of OFRFT-OFDM with EQ, DCO-OFDM with EQ, OFRFT-OFDM without EQ and DCO-OFDM without EQ at the default E_b/N_0 of 20 dB are 9.8×10^{-7}, 2.1×10^{-3}, 1.3×10^{-4} and ~ 0.01, respectively. Finally, Fig. 8 illustrates the BER performance against the E_b/N_0 for quadrature PSK (QPSK) OFRFT-OFDM and DCO-OFDM systems. Note that, 8000 OFRFT-OFDM symbols are transmitted in this case, each carrying 128 bits (64 symbols × 2 bits/symbols), and therefore 1,024,000 bits are sent for each E_b/N_0. As can be observed, for $E_b/N_0 < $ ~ 10 dB, the performance of both systems is almost the same. However, OFRFT-OFDM shows a significant improvement for higher values of E_b/N_0 compared with DCO-OFDM. For example, OFRFT-OFDM and DCO-OFDM can meet the FEC limit at E_b/N_0 of ~ 13 and 20 dB, respectively.

4. Conclusion

In this paper, we introduced an OFRFT-based orthogonal frequency division multiplexing system for visible light communications and compared it with DCO-OFDM. We showed that, OFRFT-OFDM with the optimal fractional order demonstrated a significant improvement in the BER performance compared with the DCO-OFDM system for the same computational complexity and spectral efficiency. In addition, the proposed scheme offered lower PAPR values by < 1 dB and an E_b/N_0 gain of 7 dB for the same BER compared with DCO-OFDM.
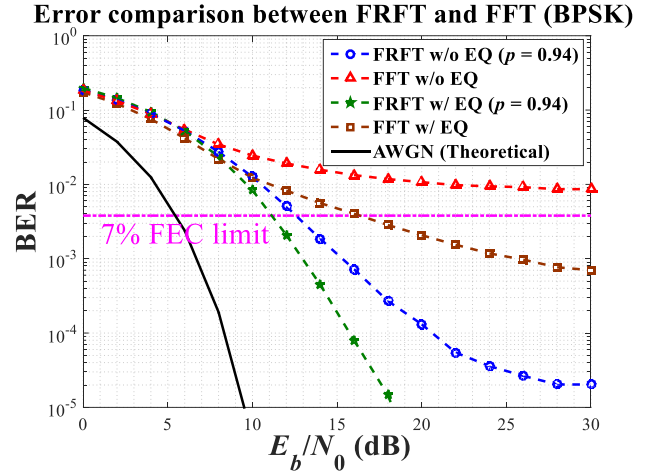

Fig. 7. The BER performance against E_b/N_0 with and without the EQ for BPSK OFRFT-OFDM and DCO-OFDM systems.
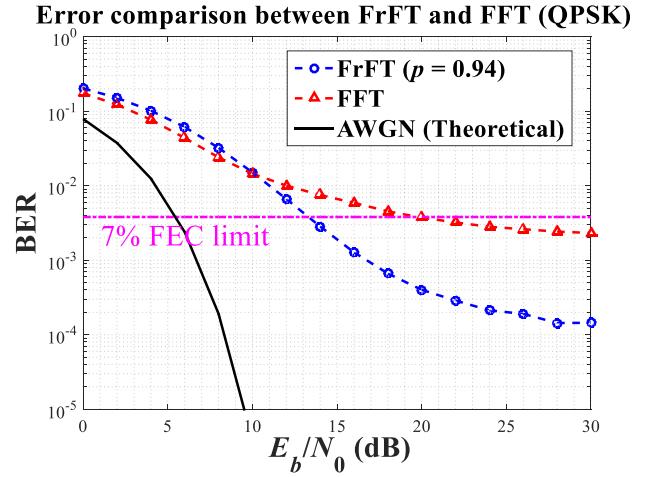

Fig. 8. The BER performance against E_b/N_0 for QPSK OFRFT-OFDM and DCO-OFDM systems.

References

1. M. Z. Chowdhury, M. T. Hossan, A. Islam, and Y. M. Jang, "A comparative survey of optical wireless technologies: Architectures and applications," IEEE Access **6**, 9819–9840 (2018).
2. Z. Ghassemlooy, W. Popoola, and S. Rajbhandari, Optical wireless communications: system and channel modelling with Matlab® (CRC press, 2019).
3. K. Sakaguchi, T. Haustein, S. Barbarossa, E. C. Strinati, A. Clemente, G. Destino, A. Pärssinen, I. Kim, H. Chung, J. Kim *et al.*, "Where, when, and

how mmwave is used in 5g and beyond," IEICE Transactions on Electron. **100**, 790–808 (2017).

4. Z. Ghassemlooy, S. Arnon, M. Uysal, Z. Xu, and J. Cheng, "Emerging optical wireless communications-advances and challenges," IEEE journal on selected areas communications **33**, 1738–1749 (2015).

5. R. Ji, S. Wang, Q. Liu, and W. Lu, "High-speed visible light communications: Enabling technologies and state of the art," Appl. Sci. **8**, 589 (2018).

6. F. Khan, S. R. Jan, M. Tahir, and S. Khan, "Applications, limitations, and improvements in visible light communication systems," in *2015 International Conference on Connected Vehicles and Expo (ICCVE),* (IEEE, 2015), pp. 259–262.

7. L. E. M. Matheus, A. B. Vieira, L. F. Vieira, M. A. Vieira, and O. Gnawali, "Visible light communication: concepts, applications and challenges," IEEE Commun. Surv. & Tutorials **21**, 3204–3237 (2019).

8. S. Al-Ahmadi, O. Maraqa, M. Uysal, and S. M. Sait, "Multi-user visible light communications: State-of-the-art and future directions," IEEE Access **6**, 70555–70571 (2018).

9. Z. Ghassemlooy, L. N. Alves, S. Zvanovec, and M.-A. Khalighi, *Visible light communications: theory and applications* (CRC press, 2017).

10. J. Armstrong, "Ofdm for optical communications," J. lightwave technology **27**, 189–204 (2009).

11. X. Wang, "Ofdm and its application to 4g," in 14th Annual International Conference on Wireless and Optical Communications, 2005. WOCC 2005, (IEEE, 2005), p. 69.

12. D. Tsonev, S. Sinanovic, and H. Haas, "Complete modeling of nonlinear distortion in ofdm-based optical wireless communication," J. Light. Technol. **31**, 3064–3076 (2013).

13. E. Chen, R. Tao, and X. Meng, "The ofdm system based on the fractional fourier transform," in *First International Conference on Innovative Computing, Information and Control-Volume I (ICICIC'06),* vol. 3 (IEEE, 2006), pp. 14–17.

14. H. Wang and H. Ma, "Mimo ofdm systems based on the optimal fractional fourier transform," Wirel. Pers. Commun. **55**, 265–272 (2010).

15. G. Cincotti, "Optical ofdm based on the fractional fourier transform," in *Next-Generation Optical Communication: Components, Sub-Systems, and Systems,* vol. 8284 (International Society for Optics and Photonics, 2012), p. 828409.

16. M. Nassiri and G. Baghersalimi, "Comparative performance assessment between fft-based and frft-based mimo-ofdm systems in underwater acoustic communications," IET Commun. **12**, 719–726 (2018).

17. A. Bultheel and H. E. M. Sulbaran, "Computation of the fractional fourier transform," Appl. Comput. Harmon. Analysis **16**, 182–202 (2004).

18. V. Namias, "The fractional order fourier transform and its application to quantum mechanics," IMA J. Appl. Math. **25**, 241–265 (1980).

19. L. B. Almeida, "The fractional fourier transform and time-frequency representations," IEEE Transactions on signal processing **42**, 3084–3091 (1994).

20. M. Martone, "A multicarrier system based on the fractional fourier transform for time-frequency-selective channels," IEEE Transactions on Commun. **49**, 1011–1020 (2001).

21. Y. Aiying and X. Chen, "Method of measuring optical fiber link chromatic dispersion by fractional fourier transformation (frft)," (2017). US Patent 9,602,199.

22. H. Zhou, B. Li, M. Tang, K. Zhong, Z. Feng, J. Cheng, A. P. T. Lau, C. Lu, S. Fu, P. P. Shum *et al.*, "Fractional fourier transformation-based blind chromatic dispersion estimation for coherent optical communications," J. Light. Technol. **34**, 2371–2380 (2016).

23. C. Hu, W. Li, Q. Feng, Q. Zheng, Y. Wang, and Y. Xie, "A novel in-band osnr monitoring technique based on fractional fourier transform of lfm signal," Opt. Commun. **445**, 36–40 (2019).

24. J. Zheng and Z. Wang, "Ici analysis for frft-ofdm systems to frequency offset in time-frequency selective fading channels," IEEE Commun. letters **14**, 888–890 (2010).

25. Z. Mokhtari and M. Sabbaghian, "Near-optimal angle of transform in frft-ofdm systems based on ici analysis," IEEE Transactions on Veh. Technol. **65**, 5777–5783 (2015).

26. A. Yang, X. Liu, and X. Chen, "A frft based method for measuring chromatic dispersion and spm in optical fibers," Opt. Fiber Technol. **34**, 59–64 (2017).

27. Y. Zhao, H. Yu, G. Wei, F. Ji, and F. Chen, "Parameter estimation of wideband underwater acoustic multipath channels based on fractional fourier transform," IEEE Transactions on Signal Process. **64**, 5396–5408 (2016).

28. H. M. Ozaktas, O. Arikan, M. A. Kutay, and G. Bozdagt, "Digital computation of the fractional fourier transform," IEEE Transactions on signal processing **44**, 2141–2150 (1996).

29. I. Venturini and P. Duhamel, "Reality preserving fractional transforms [signal processing applications]," in *2004 IEEE International Conference on Acoustics, Speech, and Signal Processing,* vol. 5 (IEEE, 2004), pp. V–205.

30. J. Lang, "The reality-preserving multiple-parameter fractional fourier transform and its application to image encryption," in *2012 5th International Congress on Image and Signal Processing,* (IEEE, 2012), pp. 1153–1157.

31. E. Chen and C. Chu, "Single-carrier fractional Fourier domain equalization system with zero padding for fast time-varying channels," EURASIP Journal on Wireless Communications and Networking. **1**, 1-10 (2014).

32. F. B. d. Silva, "Nonlinear adaptive equalization with data selection in vlc systems," Ph.D. thesis, Universidade Federal do Rio de Janeiro (2018).

33. G. Stepniak, J. Siuzdak, and P. Zwierko, "Compensation of a vlc phosphorescent white led nonlinearity by means of volterra dfe," IEEE Photonics Technol. Lett. **25**, 1597–1600 (2013).

34. W. Zhao, Q. Guo, J. Tong, J. Xi, Y. Yu, P. Niu, and X. Sun, "Orthogonal polynomial-based nonlinearity modeling and mitigation for led communications," IEEE Photonics J. **8**, 1–12 (2016).

35. H. Qian, S. Yao, S. Cai, and T. Zhou, "Adaptive postdistortion for nonlinear leds in visible light communications," IEEE Photonics J. **6**, 1–8 (2014).

36. K. Ying, Z. Yu, R. J. Baxley, H. Qian, G.-K. Chang, and G. T. Zhou, "Nonlinear distortion mitigation in visible light communications," IEEE Wirel. Commun. **22**, 36–45 (2015).

37. J. B. Carruthers and P. Kannan, "Iterative site-based modeling for wireless infrared channels," IEEE Transactions on Antennas Propag. **50**, 759–765 (2002).